

Hyper-Yoshimura: How a Slight Tweak on a Classical Origami Pattern Unleashes Meta-stability for Deployable Robotics

Ziyang Zhou^{1†*}, Yogesh Phalak^{1†*}, Vishrut Deshpande¹,
Ethan O’Brien¹, Ian Walker², Suyi Li¹

¹Department of Mechanical Engineering, Virginia Tech., Blacksburg & 24060, USA.

²Department of Electrical Engineering and Computer Science, University of Wyoming, Laramie & 82071, USA.

*Corresponding author: zzhou4@vt.edu; yphalak@vt.edu

[†]These authors contributed equally to this work.

Deployable structures inspired by origami have provided lightweight, compact, and reconfigurable solutions for various robotic and architectural applications. However, creating an integrated structural system that can effectively balance the competing requirements of high packing efficiency, simple deployment, and precise morphing into multiple load-bearing configurations remains a significant challenge. This study introduces a new class of *hyper-Yoshimura* origami, which exhibit a wide range of kinematically admissible and locally metastable states, including newly discovered symmetric “self-packing” and asymmetric “pop-out” states. This metastability is achieved by breaking a design rule of Yoshimura origami that has been in place for many decades. To this end, this study derives a new set of mathematically rigorous design rules and geometric formulations. Based on this, forward and inverse kinematic strategies are developed to stack hyper-Yoshimura modules into deployable booms that can approximate complex

3D shapes. Finally, this study showcases the potential of hyper-Yoshimura with a meter-scale pop-up cellphone charging station deployed at our university’s bus transit station, along with a 3D-printed, scaled prototype of a space crane that can function as an object manipulator, solar tracking device, or high-load-bearing structure. These results establish hyper-Yoshimura as a promising platform for deployable and adaptable robotic systems in both terrestrial and space environments.

Deployable and morphable structures — capable of transforming between compact, stowed configurations and sophisticated three-dimensional forms — are foundational to a wide range of modern engineering tasks, including orbital construction (1–4), surgical operations (5–7), and kinetic architecture (8–10). These structures can also serve as the skeleton of reconfigurable robots, making them ideal for space-efficient packing (11–13), versatile locomotion (14–19), and multi-tasking (20–24). However, despite the substantial advancements in this topic, it remains a significant challenge to create an integrated structural system that can seamlessly balance the competing requirements from different performance metrics, including efficiently packing into a small volume, rapidly deploying with minimal actuation, and precisely morphing into multiple load-bearing configurations.

In this study, we demonstrate that a slight modification of the classical *Yoshimura origami* yields a simple, modular, and versatile structural solution to address the challenge above. Yoshimaru Yoshimura first studied this origami pattern in the 1950s by observing the compression buckling pattern of cylindrical shells (25). Since then, Yoshimura origami has garnered increasing interest due to its unique folding kinematics (26–28) and structural performance (29–31). Surprisingly, all studies so far followed the same elemental design rule: the sector angle β that defines the underpinning rhombus facet shape is correlated to the number of rhombi n around its circumference, such that $\beta = 90^\circ/n$ (Figure 1). This rule ensures that the Yoshimura can fold into an ideally zero-thickness flat shape under compression (i.e., flat foldability) (32). In this study, however, we intentionally break this rule and discover that when $\beta > 90^\circ$, two novel mechanical behaviors can emerge: *self-packability* and *meta-stability* (Figure 1, Table 1). Self-packability means that the new Yoshimura origami can be axially compressed into a compact configuration that resembles a discretized hyperbolic surface. Therefore, we name this new class of origami patterns as the *hyper-Yoshimura*. Moreover, the internal stress will stabilize the origami into this hyper-folded

shape. On the other hand, meta-stability means that each hyper-Yoshimura module can settle into 2^n intermediate, asymmetrically stable equilibria between the self-packed and fully deployed states. These two behaviors, combined, create a deployable backbone structure that features highly efficient packing and massive reconfigurability without requiring complex actuation.

To this end, the rest of this paper comprises two sections that comprehensively investigate the geometric framework of hyper-Yoshimura and its implementations in deployable robotics. In the first section, we establish the kinematics basis to understand the self-packing and meta-stable potential of a hyper-Yoshimura module. We then proceed to develop forward and inverse kinematics models for stacking these modules into deployable backbones. We demonstrate the deploy-and-reconfigure ability of hyper-Yoshimura via a meter-scale, *pop-up cellphone charging station* deployed at our university’s bus transit station. In the second section, we further advance the hyper-Yoshimura concept by seamlessly combining different sector angles β into a single continuous boom. We experimentally demonstrate that such a hybrid design enables complex reconfigurations and shape control with minimal actuation (i.e., with a single set of tendons and a pneumatic pressure supply). Finally, we validate hyper-Yoshimura’s usage in deployable robotics with a multi-functional *space crane* concept that can be repurposed into a capable manipulator with expandable work space, a deployable boom to re-position and re-orient solar panels, or a load-bearing column. The outcome of this study can pave the way for a new family of high-performance deployable robotics and kinetic architectures.

1 The Emergence of Self-Packability and Meta-stability

1.1 Geometric Foundations

In this section, we introduce several important concepts in geometry and mechanics that underpin the entire study.

Yoshimura Crease Pattern and Design Variables:

The Yoshimura origami, obtained by folding a flat sheet through a prescribed set of creases, offers a rich platform for studying the interplay between geometry and mechanics. When it is flat

and unfolded, shown schematically in Figure 1(a), Yoshimura presents a periodic tessellation of mountain and valley folds that define the fundamental rhombus shapes. Here, mountain folds are creases that protrude out of the plane, while valley folds are those that fold into the plane. Each horizontal layer of rhombi serves as a basic unit, and the periodic arrangement of these units plays a critical role in shaping both the global morphology and mechanical behavior of the folded product.

In this unfolded precursor state, the valley folds have a length denoted by l , whereas the mountain folds have a length a . The tessellation resolution is characterized by two integer parameters: n , representing the number of rhombi along the circumferential direction, and m , denoting the number of rhombi layers along its height. Each horizontal layer of rhombi constitutes a *module* after folding, and thus m can also be interpreted as the number of modules stacked axially. The most critical parameter governing the tessellation's geometry is the sector angle β , which defines the angular separation between mountain and valley folds within the plane. The height of each module in the unfolded configuration is denoted by w .

For non-dimensionalization, a base length L is introduced such that $l/L = 1$, allowing all geometric quantities to be expressed relative to the valley fold length. In this study, unless otherwise noted, the valley fold length l will be treated as the reference length scale. Once n and β are specified, the entire geometry of the unfolded Yoshimura tessellation becomes uniquely determined, and quantities such as w and a can be derived consistently in terms of these fundamental parameters. For example, $w = \tan \beta$, and $a = \frac{1}{2 \cos \beta}$.

Folded State (F), Deployed State (D), and Transformation Variables

Upon folding along the mountain or valley crease and connecting the opposite edges, the Yoshimura tessellation transforms into a classical three-dimensional shape: a column-like structure with a zig-zagged surface, where each rhombus becomes a local valley (Figure 1b). We refer to this configuration as the *Folded state* (**F**) hereafter. In this state, the top and bottom boundaries of each module form an n -sided polygon, which is not necessarily regular. Notably, the side length of these polygons remains identical to the unfolded valley fold length l .

Two critical dihedral angles emerge in the folded configuration: θ_{out} , which describes the angle between adjacent outer facets at a boundary vertex, and θ_{in} , which represents the half-angle between adjacent inner facets, as illustrated in Figure 1(b). Each module thus features a total of n instances of

both θ_{out} and θ_{in} , which may be either identical or different depending on the folding and structural symmetry. Another geometric quantity introduced upon folding is the slant height d , defined as the straight-line distance between the centroids of the top and bottom boundary polygons of a module. The slant height provides an essential measure of the module's contraction or expansion during deformation and thus plays a pivotal role in the subsequent analysis of deployability and kinematic constraints. Finally, we define the tilt angle γ as the dihedral angle between the two boundary polygons of a module and the phase angle ψ between the reference x -axis and the end polygon's rotation axis. These two angles describe the asymmetric deformation of the Yoshimura.

From the **Folded State**, we can further stretch the Yoshimura and push the rhombus facets outwards, creating a load-bearing and cylindrical boom. We refer to this configuration as the **Deployed State (D)**. At this state, the original mountain and valley creases are no longer folded so that $\theta_{\text{in}} = \theta_{\text{out}} = 180^\circ$. (Indeed, transforming Yoshimura from **D** to **F** states exactly represents the compression buckling of a cylindrical shell.) In this study, we idealize the **Deployed State** by introducing longitudinal *virtual folds* so that it forms a symmetric and regular n -polygonal column.

Together, θ_{out} , θ_{in} , d , γ and ψ describe the shape transformation of Yoshimura at the **Folded** and **Deployed States**, so they are called the *transformation variables* (as opposed to the *design variables* β , n , and m). By systematically defining the relationships among these variables (detailed in Sections 1 and 2 of the supplementary text), Yoshimura can be studied as a parametric structure, wherein variations in these variables lead to a wide range of achievable geometries and mechanical responses. This parametric framework serves as the foundation for the subsequent kinematics and meta-stability analyses.

Kinematic Admissibility and Local Energy Minima:

With the geometric formulation of Yoshimura, which captures the compatibility between adjacent modules and shape transformations governed by variables β , γ , ψ , and d , it is now essential to examine the *kinematic admissibility* of different 3D shapes. Here, kinematic admissibility refers to the condition that the lengths of origami creases in Yoshimura (including mountain, valley, and virtual folds) are equal to their initial setup so that the thin sheet material is not stretched or sheared in-plane. Given that the stretching and shearing stiffness of a thin sheet is 2-3 orders of magnitude higher than out-of-plane bending stiffness (33, 34), a kinematically admissible shape also

corresponds to a local minimum in elastic potential energy. Therefore, the preservation of kinematic admissibility opens the possibility of achieving *meta-stability*—the existence of multiple distinct yet stable configurations for a given module geometry. Such metastable states enable controlled shape reconfiguration and programmable structural behavior within a shared geometric framework.

In the following analysis, we investigate the conditions under which the kinematic admissibility is achieved. We consider two key categories: the *symmetric folding* regime, where $\theta_{\text{in}} = \theta_{\text{out}}$, and the more general *asymmetric folding* case, where $\theta_{\text{in}} \neq \theta_{\text{out}}$. For each, we derive constraints on the sector angle β and identify the corresponding admissible values of the global transformation parameters γ , ψ , and d that yield elastically meta-stable shapes.

1.2 Symmetric Folding: From Deployed, Folded, to Self-Packed State

We begin by examining the case of symmetric folding, in which the inner and outer dihedral angles remain equal throughout the folding process. Let θ denote this common dihedral angle such that $\theta_{\text{in}} = \theta_{\text{out}} = \theta$ at all stages. The module starts from a fully Deployed State (**D**), where the slant height reaches its maximum value $d = w$, and the top, bottom, and midplane boundaries of a module form concentric, regular n -polygons. All creases retain their original lengths, ensuring this configuration remains kinematically admissible (elastically stable).

From this state, the module can be folded symmetrically by decreasing the angle θ while preserving the symmetry between the top and bottom boundaries. As θ decreases, the slant height d also reduces, and the structure approaches a second kinematically admissible state — the **Folded State** — where elastic energy reaches a local minimum.

Flat-Foldability of Classical Yoshimura

Kinematic admissibility of this **Folded state** requires the facets to tilt in a manner that satisfies two geometric constraints:

$$d = w \sin\left(\frac{\theta}{2}\right), \tag{1}$$

$$w \cos\left(\frac{\theta}{2}\right) = \tan\left(\frac{90^\circ}{n}\right). \tag{2}$$

Together, these equations define the range of θ corresponding to kinematically viable metastable states and relate the dihedral angle θ to the sector angle β and the resolution of the tessellation n . In particular, for real solutions of θ to exist, the sector angle must satisfy the inequality:

$$\beta \geq \frac{90^\circ}{n}. \quad (3)$$

The limiting case where $\beta = 90^\circ/n$ corresponds to Yoshimura origami’s well-known *flat-foldability condition*. Under this condition, the **F**olded state collapses completely into a flat shape, with $d = 0$, and all module boundaries align within a single plane (Figure 2a).

It’s worth noting that, in reality, the classical Yoshimura will always spring back slightly from this flat, folded shape due to the material’s bending stiffness along the creases and its non-zero thickness (Movie S1). This indicates that the elastic potential energy well near the flat-folded state is shallow.

Self-Packing of Hyper-Yoshimura

In many deployable engineering systems — such as space structures, biomedical stents, and morphing skins — the ability to achieve high expansion ratios is critical. Theoretically, the highest expansion ratio corresponds to a configuration in which the folded structure approaches zero height, i.e., $d \rightarrow 0$, which is uniquely achieved at the flat-foldable limit of classical Yoshimura origami. As derived in the previous section, this occurs at a single point in the parameter space where the fold angle satisfies $\beta = 90^\circ/n$. Under this condition, the entire module flattens into a planar state, maximizing its expansion ratio from the folded (**F**) to the deployed (**D**) state.

However, we observe that it is possible to achieve a similar degree of compaction across a broader range of geometric parameters — not just at the flat-foldable limit — by introducing a simple yet powerful geometric modification: When $\beta > \frac{90^\circ}{n}$, the Yoshimura module’s height at its folded configuration (**F**) is non-zero. However, we discovered that by twisting the boundary vertices out of the plane in an alternating up-and-down fashion, folding all the triangular facets along the virtual folds, and further compressing the structure axially, we can transform the Yoshimura into a compact “wavy” surface that bear a strong geometric resemblance to discretized models of hyperbolic surfaces with negatively curved saddle shapes (Figure 2a).

We defined the hyperfold angle ζ to capture the deviation from the flat condition, and it can be explicitly expressed in terms of the design parameters β and n as follows:

$$\cos \zeta = \frac{2 \sin^2 \left(\frac{90^\circ}{n} \right) - \sin^2 \beta}{\sin^2 \beta}. \quad (4)$$

This angle quantifies the local twist required to enable compaction where flat-foldability is not satisfied. The emergence of ζ generalizes the condition for compaction beyond the flat-foldable point. Furthermore, the inner radial position of the folds — measured as the minimum radial distance from the origin to the newly formed twisted layer — is given by:

$$r_{\text{in}} = \frac{1}{2 \tan(2\beta)} \quad (5)$$

This function exhibits a critical behavior: $r_{\text{in}} \rightarrow 0$ as $\beta \rightarrow 45^\circ$, and becomes negative for $\beta > 45^\circ$, indicating self-intersections and thus a geometric infeasibility. Hence, to ensure physical realizability of symmetric metastable configurations, β must lie strictly within the range:

$$\frac{90^\circ}{n} < \beta < 45^\circ. \quad (6)$$

We designate this entire class of Yoshimura with the extended β angle range as “Hyper-Yoshimura.” A complete summary of the parametric bounds and geometric conditions for the symmetric folding states is provided in Table 1. The formulations above also yield the correction between the sector angle β and the transformation variables, summarized in Figure 2(b-d).

Finally, it is worth highlighting that this hyperfolded and packed configuration is also kinematically admissible, meaning that it corresponds to a local potential energy minimum (i.e., a stable state). Indeed, we found the local energy minimum of the packed configuration to be much more prominent than that of the flat-folded configuration in classical Yoshimura (Figure 2a and Movie S1). This is due to the internal stress from folding the facets along the virtual creases. Indeed, one can understand such internal stress from a simple experiment: If we cut the packed hyper-Yoshimura along its virtual crease, we will essentially release such internal stress and obtain an n -polygon ring with a circumference larger than 360° (while cutting a classic Yoshimura would yield a ring with exactly 360° circumference, see Figure 2e and Movie S1). This presents a strong resemblance to joining an annular ring with a circumference of more than 360° into a wavy surface. Due to the strong local energy minima, we will refer to the compact configuration of hyper-Yoshimura as the

“self-**P**acked State (**P**).” (Here, we use the intuitive acronym “**PDF**” to represent the self-**P**acked, **D**eployed, and **F**olded states.) The self-packing behavior has strong practicality because it enables a deployable structure to compact and stow itself without the need for additional fixtures to maintain its shape.

1.3 Asymmetric Folding: Meta-stable Pop-Out States

Beyond symmetric folding configurations, the hyper-Yoshimura also supports a rich set of asymmetric metastable states, which we term *pop-out states*. These states are distinguished by the unequal distribution of dihedral angles (i.e., θ_{in} and θ_{out}) within one hyper-Yoshimura module. They can be reached by locally inverting and “popping” a rhombus outwards so that its valley folds become inactive and the virtual folds are engaged (Figure 1 and 2f) — Therefore, these pop-out states are essentially intermediate and kinematically admissible equilibria between the **F**olded and **D**eployed states, because the **D**eployed state is reached when all rhombii are popped out. Moreover, their asymmetric shapes cause the end polygons to rotate, resulting in a bending deformation.

A more careful observation of these pop-out states reveals a critical deformation pattern: When n is odd, popping out one rhombus will rotate the end n -polygons in a way to move their opposite edges towards each other. If a critical design condition is met (more on this later), these two opposite edges can coincide, causing the corresponding dihedral angle θ_{in} to reach its limit at 0° . We call this *edge-wise degeneracy*. Meanwhile, popping out two *adjacent* rhombii will rotate the end polygons in a different orientation so that only their opposite vertices can move towards each other and coincide, causing the corresponding dihedral angle θ_{out} to reach its limit at 0° . We refer to this as *vertex-wise degeneracy*. However, when n is even, this relationship is switched: 1 pop-out will cause vertex-wise degeneracies, and 2 pop-outs will cause edge-wise degeneracies. Finally, popping more than two rhombii will force the whole module towards the **D**eployed state — That it, no kinematically admissible states exist with more than two popped-out rhombii except for the **D**eployed state.

These asymmetric states are significant because they introduce new metastable states into the configuration space of the hyper-Yoshimura, expanding its functional versatility. Depending on the number and arrangement of facets that undergo this local inversion, different classes of

metastable pop-out states are possible. In what follows, we derive the design condition to ensure such asymmetric meta-stability, that is, to ensure kinematic feasibility when edge-wise or vertex-wise degeneracy occurs. For each case, we determine the limiting values of the sector angle β for *all n values*, and compute the corresponding transformation parameters (γ, ψ, d) that characterize the resulting shape.

Edge-wise Degeneracy $\theta_{\text{in}} = 0$ (1 pop-out for odd n or 2 pop-out for even n)

To examine the emergence of kinematically admissible edge-wise degeneracy, we begin by selecting an arbitrary edge from the bottom boundary polygon and its corresponding edge on the top boundary polygon. For this analysis, we set the inner dihedral angle associated with these edges to zero, i.e., $\theta_{\text{in}} = 0$, thereby enforcing geometric coincidence along that edge. Due to axial symmetry, the two outer dihedral angles adjacent to this edge — one on each side — remain equal,

To describe the geometry of this configuration, we define a length parameter λ' , which represents the farthest radial distance from the coinciding edges to the most distant vertex on either the top or bottom boundary polygons (Figure 2f). This geometric measure plays a critical role in determining the feasible values of the tilt angle γ . The value of λ' depends on whether the number of polygon sides n is even or odd:

$$\lambda' = \begin{cases} \frac{\cos\left(\frac{180^\circ}{n}\right)}{\sin\left(\frac{180^\circ}{n}\right)}, & \text{if } n \text{ is even,} \\ \frac{1 + \cos\left(\frac{180^\circ}{n}\right)}{2 \sin\left(\frac{180^\circ}{n}\right)}, & \text{if } n \text{ is odd.} \end{cases} \quad (7)$$

We also introduce an auxiliary angle η , defined as the angle at the coinciding edge in the mid-plane polygonal projection. This angle helps us describe the internal geometry of the module near the pop-out region (Figure 2f). To derive the required geometric parameters, we define four critical points in 3D space based on the Yoshimura folding framework:

$$O \equiv (0, 0, 0), \quad (8)$$

$$P \equiv \left(\frac{1}{2}, \frac{w}{2}, 0 \right), \quad (9)$$

$$Q \equiv \left(\sin \left(\frac{\eta}{2} \right), \cos \left(\frac{\eta}{2} \right), 0 \right), \quad (10)$$

$$R \equiv \left(\frac{1}{2} + \cos \left(\frac{360^\circ}{n} \right), \sin \left(\frac{360^\circ}{n} \right) \cos \left(\frac{\gamma}{2} \right) + \frac{\tan \beta}{2}, \sin \left(\frac{360^\circ}{n} \right) \sin \left(\frac{\gamma}{2} \right) \right), \quad (11)$$

where γ is the tilt angle between the top and bottom planes, and w is the unfolded height of the module. To ensure kinematic admissibility, two conditions must be satisfied. First, the vertical separation resulting from the tilt must be consistent with the virtual fold crease length w , which gives:

$$\sin \left(\frac{\gamma}{2} \right) = \frac{w}{2\lambda'}. \quad (12)$$

Second, the lengths of the segments PQ and QR must be equal to the mountain fold's length a . This gives the equation:

$$\|P - Q\| = \|Q - R\| = a, \quad (13)$$

Solving these three sets equations simultaneously yields the values of β , γ , and η that correspond to a kinematically admissible edge-wise degeneracy. The sector angle obtained in this scenario is denoted as β_{in} , which represents the lower bound beyond which θ_{in} would become negative and the popped-out configuration would cease to be kinematically admissible (Figure 2g).

The slant height d for this configuration is computed using the relation:

$$d_{\text{in}} = \frac{\sin \left(\frac{\gamma}{2} \right)}{\tan \beta}. \quad (14)$$

Although the choice of the coinciding edge is arbitrary, the regularity of the boundary polygon imposes discrete rotational symmetries on the phase angle ψ . Specifically, ψ must correspond to a rotation that aligns the coinciding edges at their centers. Thus, the allowed discrete values of ψ are given by:

$$\psi_{\text{in}}^i = \frac{360^\circ}{n}i + \frac{180^\circ}{n}, \quad i = 0, 1, \dots, n-1. \quad (15)$$

This formulation therefore gives rise to n distinct metastable configurations, each corresponding to a different choice of coinciding edge, and each governed by the same set of geometric constraints.

Vertex-wise Degeneracy $\theta_{\text{out}} = 0$ (2 pop-out for odd n or 1 pop-out for even n)

In direct analogy to the edge-wise degeneracy, we now examine a second class of asymmetric metastable states in which the module geometry collapses locally at a vertex. To analyze this case, we select an arbitrary vertex shared by the top and bottom boundary polygons and impose the condition $\theta_{\text{out}} = 0$, corresponding to a complete closure of the adjacent outer facets at that vertex.

To define the key geometric relationships in this configuration, we introduce the following critical points (Figure 2f):

$$O \equiv (0, 0, 0), \quad (16)$$

$$P \equiv \left(\frac{1}{2}, \frac{w}{2}, 0 \right), \quad (17)$$

$$Q \equiv \left(\cos \left(\frac{180^\circ}{n} \right), \sin \left(\frac{180^\circ}{n} \right) \cos \left(\frac{\gamma}{2} \right), \sin \left(\frac{180^\circ}{n} \right) \sin \left(\frac{\gamma}{2} \right) \right), \quad (18)$$

where γ again denotes the tilt angle between the top and bottom end polygons. In this configuration, the relevant diagonal distance across the regular boundary polygon, denoted λ , differs depending on whether n is even or odd:

$$\lambda = \begin{cases} \frac{1}{\sin \left(\frac{180^\circ}{n} \right)}, & \text{if } n \text{ is even,} \\ \frac{1 + \cos \left(\frac{180^\circ}{n} \right)}{2 \sin \left(\frac{180^\circ}{n} \right)}, & \text{if } n \text{ is odd.} \end{cases} \quad (19)$$

To ensure kinematic admissibility, we apply two constraints. First, same as in the previous case, the vertical rise associated with the tilt angle must correspond to the unfolded module height w , yielding:

$$\sin \left(\frac{\gamma}{2} \right) = \frac{w}{2\lambda}. \quad (20)$$

Second, the length of the fold lines must remain unchanged after folding, which gives:

$$\|P - Q\| = a, \quad (21)$$

where a denotes the mountain fold length, which is a function of β . Solving these equations simultaneously allows us to determine the critical values of β_{out} and γ_{out} that support the vertex-wise degeneration. The corresponding slant height d can be obtained from the side-view projection using triangle similarity arguments, yielding:

$$d_{\text{out}} = \frac{\sin\left(\frac{\gamma}{2}\right)}{\sin\left(\frac{180^\circ}{n}\right)}. \quad (22)$$

As in the one-facet pop-out case, the rotational symmetry of the boundary polygon restricts the phase angle ψ_{out} to discrete values that align each coinciding vertex. Specifically,

$$\psi_{\text{out}}^i = \frac{360^\circ}{n}i, \quad i = 0, 1, \dots, n-1. \quad (23)$$

This formulation introduces n additional metastable configurations, each corresponding to a distinct vertex coincidence.

Figure 2(g-i) summarizes threshold values of sector angle β , tilt angle γ , and sleight height d to achieve kinematically admissibility at edge- and vertex-wise degeneracies. These formulations above apply to any n values. Among these, the threshold values for sector angle β are the most important because they determine the underpinning hyper-Yoshimura design, and all other variables are dependent on β . Usually, the threshold β values for edge- and vertex-wise degeneracy (i.e. β_{in} and β_{out}) differ slightly from each other for the same n . This holds for every n except for the unique case when $n = 3$, when $\beta_{\text{in}} = \beta_{\text{out}} = 31.72^\circ = \cot^{-1} 1.618$, which is the golden ratio angle. Our previous study thoroughly examined the emergence of this golden ratio angle (35).

These kinematically admissible edge- and vertex-wise degenerate states significantly enrich the metastable landscape of hyper-Yoshimura. Each introduces a family of discrete, physically realizable configurations indexed by polygonal symmetry, with transitions governed by geometric collapse at edges or vertices. Unlike the symmetric **D**eployed, **F**olded, and self-**P**acked States, which preserve uniformity across the origami structure, these asymmetric states demonstrate the structure's ability to localize deformation, enabling a broader spectrum of deployable and morphing behaviors. In

total, the $2n$ pop-out configurations— n per mechanism—highlight the combinatorial richness and tunability of hyper-Yoshimura when mechanical constraints are tightly coupled with geometric modularity.

2 Deployment and Reconfiguration of Modular hyper-Yoshimura

Thus far, we have identified and characterized the metastable states within a single hyper-Yoshimura module, including both symmetric (i.e., **F**olded, **D**eployed, and self-**P**acked configurations) and asymmetric pop-out states (edge-wise and vertex-wise degeneracy).

Among all the configurations, the self-packing (**P**) offers the highest compaction ratio. However, it forces all Yoshimura modules to take the same spatial footprint and does not directly contribute to the ability to reconfigure. In contrast, the deployed (**D**) and folded (**F**) states, along with the $2n$ asymmetric pop-out states (one for each edge and vertex), are the primary contributors to large-scale geometric reconfiguration. When Yoshimura modules settle in any one of these $2 + 2n$ meta-stable states, one can tile them seamlessly via the n -polygon end opening without violating the kinematic admissibility. As a result, the total number of global configurations grows *combinatorially* with the number of modules. Specifically, a hyper-Yoshimura boom composed of m modules can theoretically access up to $(2 + 2n)^m$ distinct global configurations. Such exponential growth enables a surprisingly large shape configuration space, even for a relatively small number of modules.

In this section, we analyze the kinematic configuration space of a hyper-Yoshimura boom. We investigate how this configuration space evolves with changes in design parameters n and m , and we classify the resulting shapes generated by stacking different modules. Finally, we propose a strategy for shape approximation: fitting a hyper-Yoshimura boom to a desired target geometry via a sequence of metastable state selections.

2.1 Forward Kinematics

To analyze the global geometry of a hyper-Yoshimura boom, we apply the homogeneous transformation matrix denoted $T_{top \leftarrow bottom}(d, \gamma, \psi)$, which maps the bottom end polygon of a module to its top end (Sections 1, 2 of the supplementary text). As discussed earlier, the only dimensional quantity in this transformation is the slant height d . To maintain consistency across modules of

different geometries, we non-dimensionalize all modules by scaling with the circumradius r of the regular boundary polygon. Consequently, the transformation matrix for the i^{th} module becomes:

$$T^{(i)} = T_{top \leftarrow bottom} \left(\frac{d_i}{r}, \gamma_i, \psi_i \right), \quad (24)$$

where the parameters γ_i , ψ_i , and d_i define the geometry of the i^{th} module in its current metastable state. To compute the global configuration of a stacked boom, we adopt a recursive approach. We place the bottom boundary of the first module at the origin, such that the initial position vector, corresponding to the centroid of this bottom end polygon, is given by $\mathbf{x}_0 = [0 \ 0 \ 0 \ 1]^\top$. The centroid position of the top end polygon of the i^{th} module, denoted \mathbf{x}_i , is then determined by the product of successive transformation matrices $\mathbf{x}_i = T^{(1)}T^{(2)} \dots T^{(i)}\mathbf{x}_0$ for $i = 1, 2, \dots, m$, where m is the total number of modules in the hyper-Yoshimura boom. This recursive formulation enables us to construct the global shape of the boom from a sequence of local state selections, providing the foundation for both visualizing the overall configuration space and solving inverse design problems.

The tree-like plot in Figure 3(a) illustrates the configuration space of a hyper-Yoshimura module with $n = 3$, where the bottom node presents the centroid of the bottom end polygon, and all other nodes presents the positions of the top polygon centroid at different meta-stable states, and there are $((2 + 2 \times 3)^1 =) 8$ top nodes. By repeating and assembling this tree plot of a single module, we can build up a “fractal tree” to represent the metastable configuration space of a stacked hyper-Yoshimura boom.

To illustrate the rapid growth of this configuration space enabled by metastability, we simulate and visualize the resulting fractal tree for values $n = 3, 4, 5, 6$, each under increasing numbers of stacked modules. These configurations, generated by enumerating all possible combinations of metastable states, are shown (Figure 3b,c, and Movie S2). The figure highlights both the geometric richness and scalability of the hyper-Yoshimura system, even with relatively small values of n and m . Interestingly, when n is odd, the fractal tree fills out the 3D configuration space more evenly; when n is even, the corresponding fractal tree converges more to a few layers of “canopies”, each shaped like a convex n -polygonal surface.

2.2 Inverse Kinematics

Unlike traditional kinematic systems with continuous degrees of freedom, the hyper-Yoshimura boom operates over a discrete configuration space. Each module exists in one of several metastable states — 2 symmetric and $2n$ asymmetric per module — resulting in a finite but exponentially growing number of total configurations. Consequently, the inverse kinematics problem is fundamentally combinatorial: given a desired target curve in 3D space, determine the optimal sequence of module states (γ_i, ψ_i, d_i) such that the resulting hyper-Yoshimura boom approximates the curve as closely as possible.

Since each metastable state maps directly to a transformation matrix $T^{(i)} = T(d_i/r, \gamma_i, \psi_i)$, the whole shape of the boom is defined by a cumulative product of these matrices as described earlier. To solve the inverse problem, we define an error metric that quantifies the deviation between the resulting backbone of the boom and the desired target geometry. Specifically, we minimize the *root-mean-square (RMS)* distance between the computed centroid $\{\mathbf{x}_{\text{boom}}^{(i)}\}_{i=1}^m$ of the top polygon of each module and a sequence of points $\{\mathbf{x}_{\text{target}}^{(i)}\}_{i=1}^m$ which are on the target curve at minimum distance from the corresponding boom points:

$$\text{RMS Error} = \sqrt{\frac{1}{m} \sum_{i=1}^m \left\| \mathbf{x}_{\text{target}}^{(i)} - \mathbf{x}_{\text{boom}}^{(i)} \right\|^2}. \quad (25)$$

The goal of inverse kinematics is thus to search over all valid combinations of metastable states (i.e., state vectors of length m , where each entry is one of the $2 + 2n$ options) to find the configuration that minimizes this error metric. Given the discrete nature and exponential growth of the total configuration space, exact solution via *exhaustive search* becomes intractable for large values of m and n . For example, with $n = 4$ and $m = 10$, the total number of possible configurations is already $(2 + 2 \times 4)^{10} = 10^{10}$. However, techniques from combinatorial optimization and computer science offer practical approaches for exploring this space. For example, for small values of n and m , it is still computationally feasible to use the *Exhaustive Search* method to enumerate all configurations and select the global optimum. For higher n and m values, one can use *Greedy Algorithms*, which select a locally optimal state at each module step to minimize the cumulative error incrementally. While not guaranteed to find the global minimum, greedy strategies often yield good approximations in practice (36,37). One can also use *Dynamic Programming* to reformulate the

problem to exploit overlapping subproblems, especially when constraints or similarity exist across modules. This enables the reuse of partial computations and the efficient pruning of suboptimal branches (38). One can also use heuristic-guided methods, such as *Beam Search* and *k-Best Search*, to explore only the top k promising configurations at each module, thereby balancing solution quality and computational cost (39). Additionally, in many practical scenarios, it is sufficient to find locally optimal configurations. This can be done by limiting the search space to subsets of modules (e.g., optimizing over sliding windows of 2–4 layers), which dramatically reduces complexity while still producing close fits to the target shape.

In Figure 3(d), we illustrate several representative 3D curves — including circle, parabola, and spiral — alongside their best-fitting hyper-Yoshimura boom approximations computed via the Exhaustive Search method or Greedy Algorithms. For the *circle*, we used the parametric equations $x(t) = 0$, $y(t) = r \cos\left(\frac{wt}{4}\right) - r$, and $z(t) = r \sin\left(\frac{wt}{4}\right)$, where $r = 1.0$ and $w = \frac{8\pi}{t_{\max}}$. The *parabolic* curve is defined as $x(t) = 0$, $y(t) = -0.6t^2$, and $z(t) = t$. For the *spiral*, we used $x(t) = -2.0t$, $y(t) = r \cos\left(\frac{wt}{4}\right) - r$, and $z(t) = r \sin\left(\frac{wt}{4}\right)$, with $r = 2.0$ and the same angular frequency $w = \frac{8\pi}{t_{\max}}$. These results demonstrate that, despite operating over a discrete state space, the hyper-Yoshimura offers rich expressiveness and surprising shape versatility, especially as the number of modules increases.

3 Hyper-Yoshimura Pop-up Phone Charger: Shape Reconfiguration Demonstration

3.1 Assembling a Meter-Scale hyper-Yoshimura Boom

To demonstrate the shape re-configurability and the scalability of hyper-Yoshimura, we created a meter-scale prototype using cost-effective yet precise manufacturing techniques (Figure 3e,f). This prototype utilizes laser-cut, high-density polyethylene (HDPE) sheets as the triangular facets, each with a base crease length of $a = 61\text{cm}$. The sector angle is set at the golden ratio angle $\beta \approx 31.72^\circ$ — the threshold value to obtain asymmetric meta-stability with $n = 3$. These triangular facets are then connected with 3D-printed hinges using carbon-fiber-reinforced polylactic acid (PLA-CF) filament (Bambu Lab X1C). Heat-set inserts are directly embedded into the plastic sheets for

hinge assembly; this way, the gaps between the triangular facets can be minimized to preserve the hyper-Yohsimura's kinematic properties. Note that the locations of these hinges are critical to maintain meta-stability: In this prototype, we place them at one-third intervals along the cross creases, mirrored symmetrically around the perpendicular bisector through the midpoint of the base creases.

Following the successful assembly of a single module, four identical hyper-Yoshimura modules are stacked into a deployable boom, which has a total height of 160 cm in the **Deployed** state and only 20 cm in the self-**Packed** state (Movie S3). The whole assembly consumes 180 hinges and 720 screws, yet remains easy to disassemble and reconfigure. This is because each facet and hinge operates like a modular LEGO piece — allowing the structure to be packed, transported efficiently, and reused across different installations.

3.2 Pop-Up Solar Charging Station Demonstration

We deployed the meter-scale hyper-Yoshimura boom as a solar-powered pop-up cellphone charging station at our university's bus transit center (Figure 3g). Thanks to its lightweight construction, the structure can be easily transported in its self-packed configuration and deployed manually on-site. Three solar panels were mounted on the top layer to provide off-grid power for students needing to charge their cell phones throughout the day while waiting for buses. As the sun moved from east to west—from 9:00 AM to 8:00 PM — the top two Yoshimura modules could be manually reconfigured to track the sun's position. For instance, around noon, when the sun was directly overhead, the top Yoshimura module was set into the **Folded** state to orient the solar panels vertically, maximizing direct exposure. By selectively folding the top modules into asymmetric pop-out metastable states, the upper portion of the structure could be tilted to align with the sun's angle at different times of day, thereby optimizing solar energy capture and charging efficiency. This setup demonstrates the Yoshimura structure's practical potential as a flexible, adaptive energy-harvesting kiosk in public environments.

4 Hybrid Yoshimura Design and Sequential Buckling

Despite the rich meta-stability and shape reconfiguration ability, the hyper-Yoshimura we have studied so far uses a homogeneous pattern (i.e., β and n are the same in the origami boom). Therefore, we explore the mechanical behavior of a *hybrid* Yoshimura with a 3D-printed sample composed of three modules ($n = 3$, $m = 3$), each with a different β angle ($\beta = 30^\circ$, 31.72° golden ratio angle, and 35° from top to bottom (Figure 4a,b, full fabrication details in Section 6 of the supplementary text). This sample features thin and flexible TPU95A in the crease regions and relatively stiff Nylon materials in the facets (Ultimaker S5 FDM). All other geometric parameters—including facet dimensions and material thickness—are held constant across the three modules to isolate the effect of different β angles on mechanical response. In addition, we append half-length Yoshimura modules to both ends of the sample, allowing the installation of end caps to constrain the boundary deformation during testing. This design minimizes boundary effects so that the mechanical response is attributed primarily to changes in sector angle β .

It is important to note that, due to the finite material thickness (0.6mm at the crease and 1.4mm at the facets), the meta-stability of this 3D-printed sample deviates slightly from the ideal kinematic predictions from the previous section. While the top $\beta = 35^\circ$ module still demonstrates the symmetric self-packability, the middle $\beta = 31.71^\circ$ module does not show a clear self-packing because it is very close to the classical Yoshimura design ($\beta = 30^\circ$). This observation directly correlates to the tensile and compression testing results discussed below.

During the tensile test, the Yoshimura was stretched from being fully compressed to the fully Deployed state, reaching a total displacement of 105mm. As shown in Figure 4(c), the corresponding force–displacement curve reveals two sets of distinct snapping events (drops in the reaction force curve) that highlight the influence of different modules. The first local snap occurs between points *i* and *ii*, at a displacement range of approximately 24–34mm. This snap corresponds to the sudden “unpacking” of the bottom Yoshimura module ($\beta_3 = 35^\circ$). This is a result of the rapid release of elastic energy when this module transitions from a self-Packed (**P**) to a Folded (**F**) state. The second set of snapping events, starting between points *iii* and *iv* at around 82mm of displacement, marks the transition from Folded (**F**) to Deployed (**D**) states. This snap starts when the top layer of rhombii facets pops out, releasing the energy built up during extension. Once this initial release

occurs, the remaining layers of rhombii facets pop out sequentially from top to bottom.

Figure 4(d) shows the force–displacement response of the hybrid Yoshimura sample under quasi-static compression. The reaction force curve also exhibits a sequence of distinct peaks and drops, each corresponding to a local buckling event when a layer of rhombii facets switches from **Deployed** to **Folded** states. Notably, the top module featuring the smallest β angle always buckles first, initiating the cascading collapse. The buckling sequence progresses from top to bottom, with each pop-in event marked by a sharp drop in reaction force (points *i* to *viii*). The only exception is the final drop between points *viii* and *ix*: This correlates with the self-packing of the bottom $\beta = 35^\circ$ module.

These sequential snaps in these compression and tension tests highlight the influence of the β angle on structural response. That is, the Yoshimura modules with smaller β angles are easier to switch between **Folded** and **Deployed** stages. This allows us to use minimal actuation to transform the hyper Yoshimura for robotic applications, as detailed in the example of a deployable robotic crane below.

5 Hyper-Yoshimura Space Crane: Deployment and Robotics Demonstration

A hyper-Yoshimura boom, featuring a hybrid design, can serve as a novel alternative to conventional crane systems. Its inherent meta-stability and reconfigurability enable a range of deployment and maneuvering functions that are unattainable with traditional designs. Here, we demonstrate these functions by a deployable and robotic crane concept, which is ideal for extraterrestrial habitat construction — hence the nickname “hyper-Yoshimura space-crane” — but also shows potential use in smaller-scale biomedical applications or day-to-day human-robot collaborative operations.

Taking lessons from the aforementioned mechanical tests, we fabricate a larger scale hyper Yoshimura boom with six modules ($n = 3, m = 6$), the top three modules features the golden ratio sector angle $\beta = 31.72^\circ$, and the bottom three modules has $\beta = 35^\circ$ (Sections 3-6 of the supplementary text detail the intermediate design optimization that helped us arrive at the final design of this larger Yoshimura boom. Sections 8 and 9 detail its sequential deployment/buckling

behaviors under axial load.)

This Yoshimura boom was then integrated with simple pneumatic and tendon actuation. More specifically, three tendons, routed through top and bottom tendon locators, are anchored to servo motors mounted on a rotating disk. When activated, these motors pull the tendons and compress the hyper Yoshimura trunk to induce pop-in buckling at the rhombus facets towards the self-Packed state. In contrast, a pneumatic air tube connected to an external compressor delivers pressurized air into the boom, causing the facets to pop out sequentially towards Deployed state. Therefore, the combined use of internal pressurization and tendon actuation allows for precise and bidirectional transitions between different states. Finally, a modular upper cap design with magnetic inserts will enable us to rapidly attach different add-ons for different robotic tasks (Figure 5a and Section 10 of the supplementary text).

5.1 Configuration Switching with Minimal Actuation

Mechanical testing suggests that the space crane Yoshimura boom features six symmetric stable configurations. The top three modules with $\beta = 31.72^\circ$ can settle in the Folded (**F**) and Deployed (**D**) state, while the bottom three modules with $\beta = 35^\circ$ can settle in **F**, **D**, and self-Packed (**P**) state. For clarity, we label these six stable configurations using pairs of **P**, **D**, and **F** acronyms. For example, “[**FP**]” means the top three $\beta = 31.72^\circ$ modules are in **F**olded state and the bottom three $\beta = 35^\circ$ modules are in self-Packed state. Altogether, there are six symmetric stable configurations [**FP**], [**FF**], [**FD**], [**DP**], [**DF**], and [**DD**].

We demonstrate that, with a simple combination of pneumatic and tendon actuation, one can switch the Yoshimura boom between all these six stable configurations (Figure 5b and Movie S9). Generally speaking, pneumatic pressure can push the hyper-Yoshimura from the more compact **P** state to the extended **F** and **D** state, while tendon pulling can achieve the opposite effect. Carefully controlling the input air volume and tendon length allows the Yoshimura boom to be directed to the targeted configurations. In the configuration switch diagram shown in Figure 5(b), red arrows represent transitions driven by pneumatic pressurization, where air is pumped into the hyper-Yoshimura trunk to deploy the structure. Orange arrows indicate tendon-driven compression, where tendon pulling compresses the trunk and induces rhombus pop in transitions. In some scenarios, a

configuration switch can be achieved with a single actuation input. For example, transitioning from Folded-Folded **[FF]** state to Deployed-Folded **[DF]** state only requires a pneumatic pressure input. On the other hand, transitioning from the same **[FF]** to a different **[FD]** would require a significant pneumatic input to the **[DD]** state first, followed by a tendon pulling back into **[FD]** state.

It is worth noting that the only configuration switch requiring additional input is from **[FD]** to **[FF]**, where we must first manually pop in the lowest two layers of rhombus facets and then the tendon pulling can finish the rest of the transition (black dashed line in Figure 2b). It is also worth noting that once the hyper-Yoshimura trunk settles into the targeted configuration, we can pull the tendons differentially to bend the flexible section(s) for different robotic tasks. To this end, four configurations — **[FF]**, **[DF]**, **[DP]**, and **[FD]** — are maneuverable and can support such operations. The differential tendon pulling is controlled with an Arduino R4 platform, which integrates joystick input, command buttons, and a four-digit display to manage motor actuation, gripper operation, and real-time operations (control setup detailed in Section 11 of the supplementary text).

5.2 Demonstration 1: Deployable Manipulation with Expandable Workspace

To demonstrate the versatility of the hyper-Yoshimura Space Crane as a manipulator, we attach the gripper to the end tip of the boom to perform a series of object handling tasks across different working spaces (Figure 5d). Unlike many conventional manipulators that have a fixed length and thus operate within a fixed reachable workspace, the Yoshimura space crane dynamically adjusts its working area by transitioning between distinct stable configurations. In this demonstration, three objects were placed at different heights, requiring the crane to adapt its length to access each target. First, the crane remained in its initial folded and packed **[FP]** configuration to grip and relocate the nearest object (Movie S4). Then, the trunk transitions from the **[FP]** to an elongated **[FF]** configuration with a simple pressurization, allowing it to expand its reachable workspace and manipulate the second object positioned at a higher height (Movie S5). Finally, an additional transition from **[FF]** to a **Deployed-Foldable [DF]** configuration enables the crane to grasp and relocate a third object placed at an even greater height (Movie S6). After each object relocation, the hyper-Yoshimura boom can retract back to its initial configuration, readying itself for the next round of tasks. This retraction capability highlights the crane’s ability to reset its configuration autonomously through tendon

actuation and pneumatic control, ensuring consistent and repeatable operations. Interestingly, we also discover that the third **[DF]** configuration, despite its most extended length, is relatively easier to control due to its articulated nature: The **Deployed** modules near the tip are stiff, while the flexible **Folded** modules are near the base, so it is easier for the tendon to position the end gripper at the desired location. Overall, this demonstration showcases how reconfigurable stable states enable the hyper-Yoshimura Space Crane to reach multiple workspaces and to articulate itself into easier-to-control configurations, thus accommodating different manipulation task requirements.

5.3 Demonstration 2: Solar Panel Re-Positioning and Re-Orientation

This demonstration is inspired by the deployable and controllable solar panel assembly for the future lunar surface habitat (40, 41). The hyper-Yoshimura Space Crane enables dynamic positioning of an attached solar panel through both rotational maneuvers and structural reconfiguration (Figure 5e). In the initial **Folded and Packed [FP]** state, the crane retains sufficient flexibility to rotate the solar panel without changing its vertical position, allowing fine-tuned orientation control. To further extend its reach (e.g., due to seasonal changes in the sun position), the boom can first deploy into the fully deployed **[DD]** configuration through pneumatic actuation and is then actively compressed into the flexible and deployed **[FD]** state by motor-driven tendon pulling. In this **[FD]** state, the solar panel is now anchored at a much higher location, but the space crane maintains its rotational flexibility (Movie S7). This demonstrates the practicality of the hyper-Yoshimura structure for energy harvesting applications, where the solar panel can be continuously reoriented to track dynamic light sources, ensuring optimal energy collection even as environmental condition evolves.

It is worth noting that the solar panel re-orientation here operates differently from the meter-scale cellphone charging station discussed earlier. The charging station re-orient its solar panels by settling into asymmetric pop-out stable states. In contrast, the space crane here only bends slightly *before* reaching these asymmetric meta-stable states. Indeed, one could continue pulling a tendon on the hyper-Yoshimura space crane, bending the boom further, until the opposite facets pop out. Therefore, these two approaches to solar panel re-orientation can complement each other in practical implementations.

5.4 Demonstration 3: Load-Bearing Capability of the Yoshimura Space Crane

The hyper-Yoshimura Space Crane also exhibits excellent load-bearing capabilities without requiring continuous pneumatic pressurization (Figure 5e). For example, we transition the hyper Yoshimura crane from the **[FP]** state to the fully deployed **[DD]** configuration, and place a 5.7-kilogram weight on the top end of the structure. The hyper Yoshimura boom, despite weighing only 0.2 kilograms, managed to support this end weight without any facet buckling. This results in a load-to-weight ratio of nearly 28.5. This performance exceeds the typical ratios found in 3D-printed deployable trunk or similar lightweight robotic structures (23, 42), highlighting the mechanical efficiency and practical robustness of the Yoshimura-based design for future space or terrestrial deployment scenarios (Movie S7).

These demonstrations collectively highlight the hyper-Yoshimura Space Crane’s ability to dynamically reconfigure its structure for manipulation, rotation, and load-bearing tasks. It is essential to note that many of the delays observed during the demonstrations are primarily due to manual control switching by the human operator, rather than any mechanical limitations inherent in the structure itself. With the future integration of a feedback control system, the crane is expected to achieve significantly smoother and more continuous operation.

6 Discussion

In summary, we show that by intentionally violating a decades-old design rule for Yoshimura Origami and letting the sector angle $\beta > 90^\circ/n$, two new groups of kinematically admissible and locally stable configurations emerge: the symmetric self-**P**acked state resembling a discrete hyperbolic surface — hence the name “hyper-Yoshimura” — and the asymmetric edge-wise or vertex-wise degeneracy states (or pop out states). As a result, an ideal hyper-Yoshimura boom with negligible material thickness, n rhombii facets along its circumference, and m modules along its length can settle into $(2 + 2n)^m$ meta-stable states, each with a unique 3D shape. This study presents a mathematically rigorous design rule and kinematics formulation of the hyper Yoshimura with any n values. We also demonstrate, via numerical simulation and a meter-scale pop-up cellphone

charging station prototype, that the hyper-Yoshimura boom can exhibit massive reconfigurability, capable of matching complex target curves with relatively small n and m values, despite its discrete and combinatorial nature.

Building upon these results, we further explore a hybrid design that features a Yoshimura boom with different sector angles β along its length span. Mechanical axial compression and extension tests reveal that one can program the *sequence* of local pop-in or pop-out snaps with minimal and global actuation. Therefore, we 3D-printed a robotic, hyper-Yoshimura space crane prototype that can switch between its six symmetric stable configurations by a combination of simple pneumatic pressurization and tendon pulling. By strategically exploiting such an autonomous configuration switch and additional tendon-driven bending, the hyper-Yoshimura space crane can multi-function as (1) a capable manipulator with an expandable workspace, (2) a deployable boom that can re-orient and re-position solar panels at its top.

It’s worth noting that the shape reconfiguration in our pop-up cellphone charging station is done manually, and the combined pneumatic and tendon actuation cannot yet provide full access to all $(2 + 2n)^m$ meta-stable states in the hyper-Yoshimura boom. More capable robotic and autonomous deployment and reconfiguration would be an interesting research topic in the future. To this end, one can embed responsive materials (43, 44) — such as shape memory materials — in the origami substrate to achieve self-folding, or use distributed external actuators like pneumatic pouches (45, 46). Nonetheless, this study presents a fundamentally new class of multi-stable and robotic origami with unique multi-function capability.

7 Figures and Tables

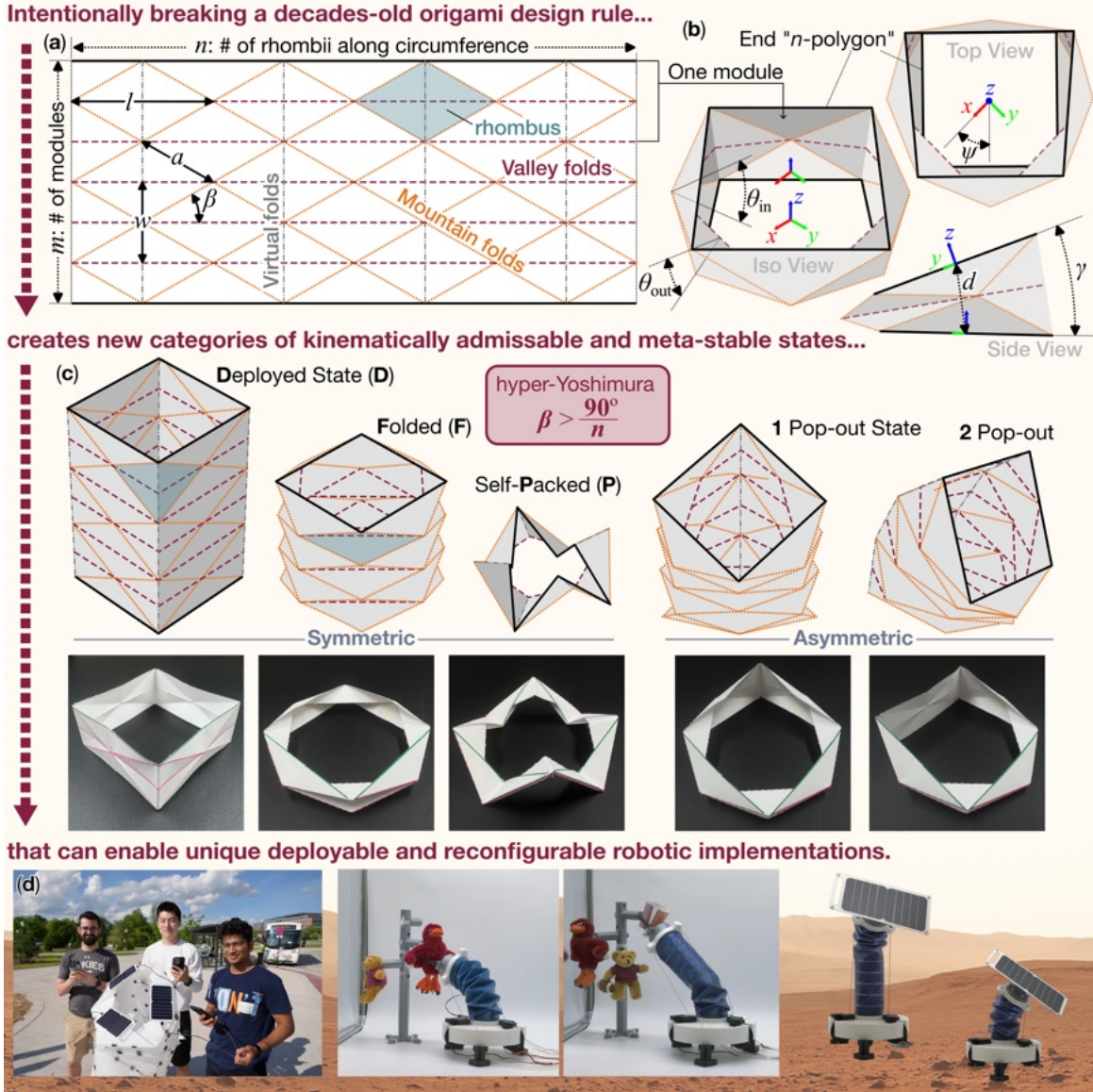


Figure 1: An overview of this hyper-Yoshimura study. (a) The underlying crease pattern, highlighting the independent *design variables* β , m , and n . (b) The 3D geometry of a slightly bent Yoshimura at its Folded state (F), highlighting the *transformation variables* θ_{in} , θ_{out} , d , γ , and ψ . (c) The three categories of metastable states and their corresponding physical realization, including the symmetric Deployed, Folded, and self-Packed states, and asymmetric 1-popout and 2-popout states. (d) The physical demonstrations of this study include a pop-up cellphone charging station, a robotic gripper with reconfigurable workspace, and a deployable boom that can reposition and reorient solar panels.

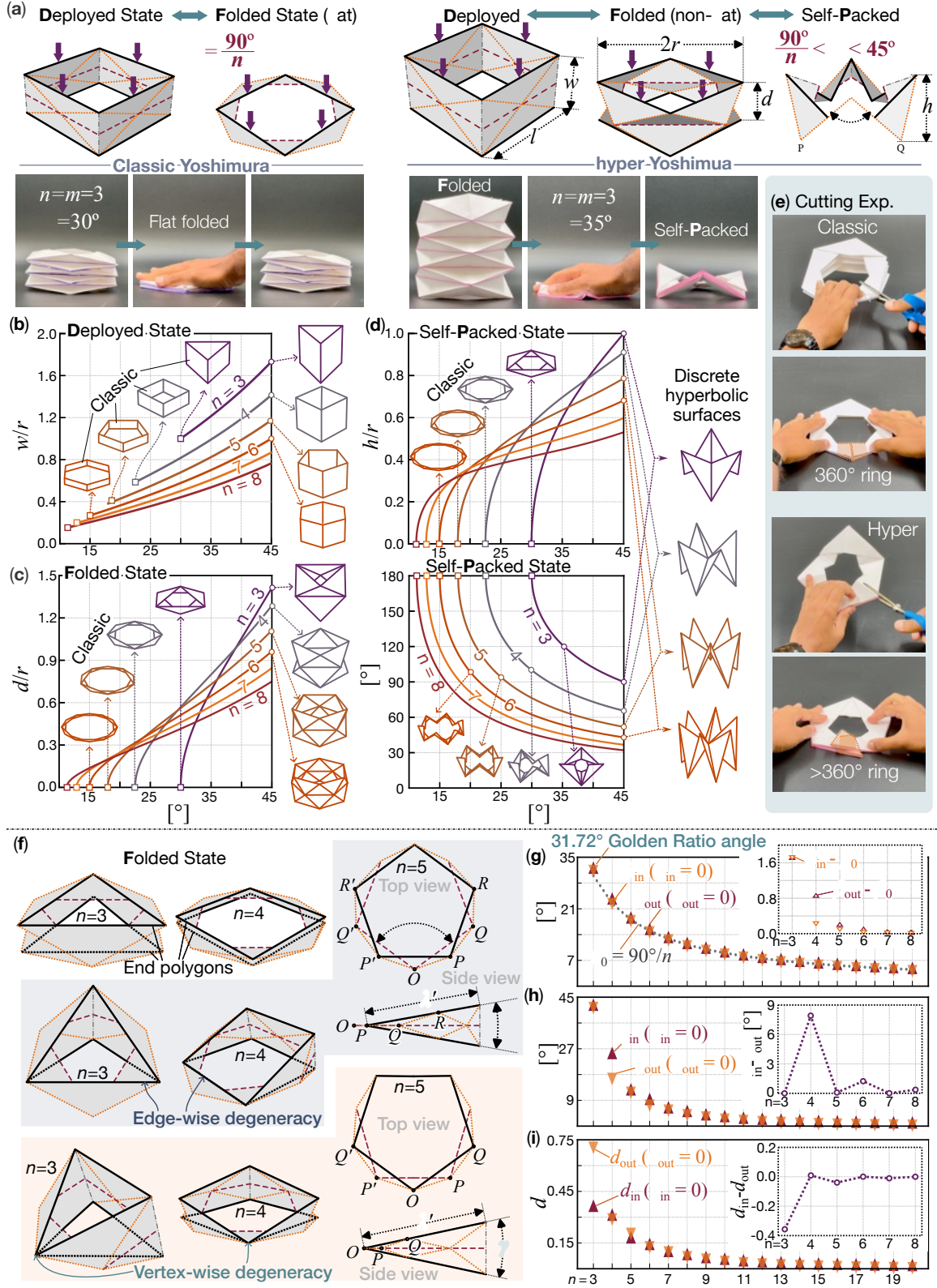


Figure 2: Meta-stability of hyper-Yoshimura.

(a) The comparison between the classic Yoshimura and the hyper-Yoshimura when they are com-

pressed axially. The self-packing behavior allowed the hyper-Yoshimura to settle into a compact volume without “springing back.” (b-d) The correlation between the sector angle β and different geometric variables, including the module’s height at the **D**eployed, **F**olded, and self-**P**acked state (w , d , and h , respectively), as well as hyper folding angle ζ . Note that the classical Yoshimura designs is represented as the squares at the end of each curve. (e) Cutting experiment explaining why the self-**P**acked state is stable. (f) The 3D geometry of a hyper-Yoshimura module at the symmetric **F**olded as well as the asymmetric edge-wise and vertex-wise degeneracy state, using $n = 3, 4$, and 5 as the examples. (g-i): The critical sector angle β_{in} , β_{out} at different n values and their corresponding tilt angle γ and sleight height d values.

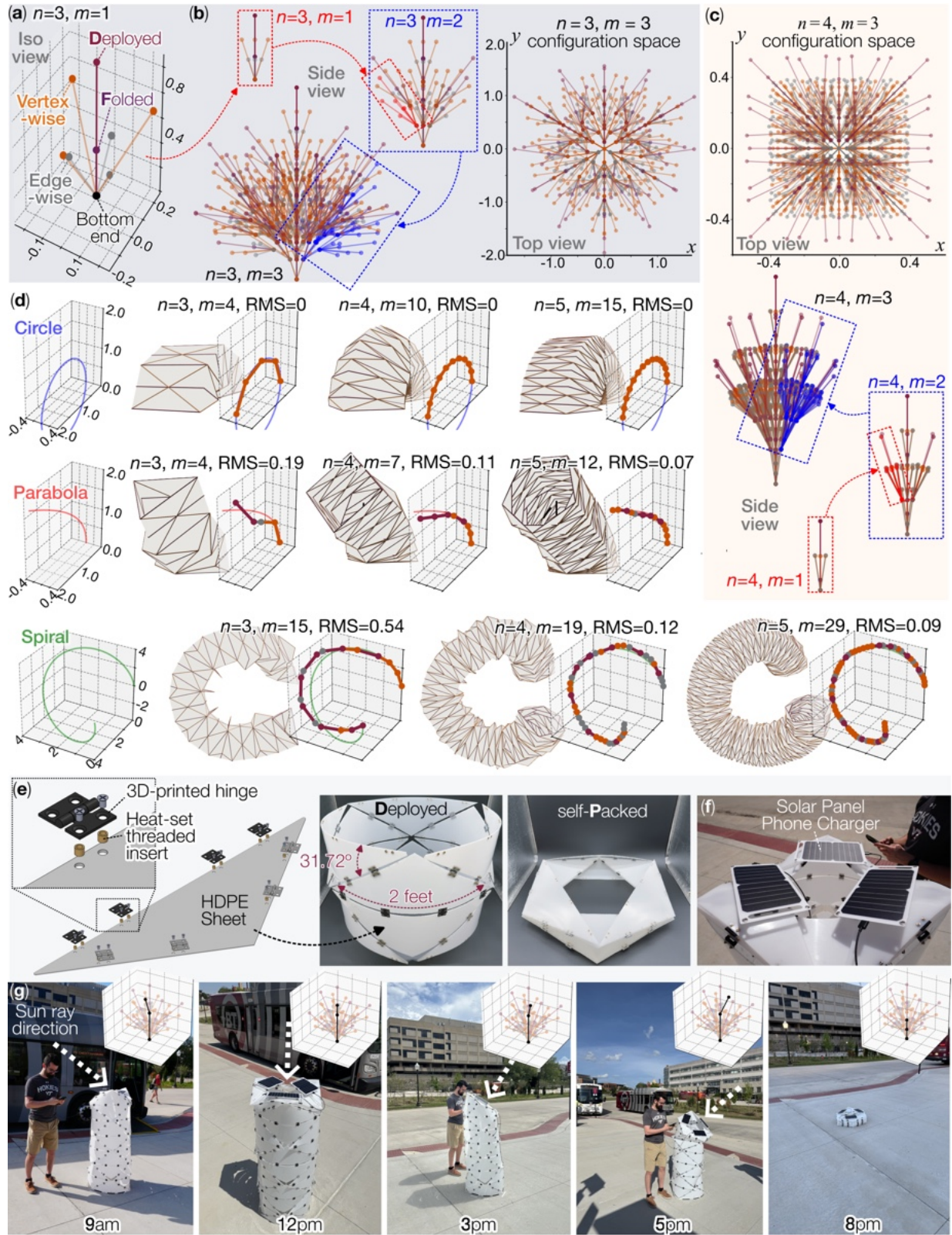


Figure 3: The rich deployment and reconfiguration capability of the hyper-Yoshimura boom.

(a) The configuration space of a single module with $n = 3$. (b) The configuration fractal tree plot

for $n = 3$ and $m = 1, 2$, and 3 , showing both side view and top view. (c) The fractal tree for $n = 4$ and $m = 1, 2$, and 3 . (d) Inverse kinematics results that configure the hyper-Yoshimura boom with different n and m values to a circle, parabola, and spiral curve. (e,f) Fabrication and assembly of the meter-scale pop-up cellphone solar charging station ($n = 3, m = 4$). (g) The charging station is deployed at the university bus transit center and reconfigured to align with the sun's direction. The small insert highlights its kinematic state within the fractal configuration tree.

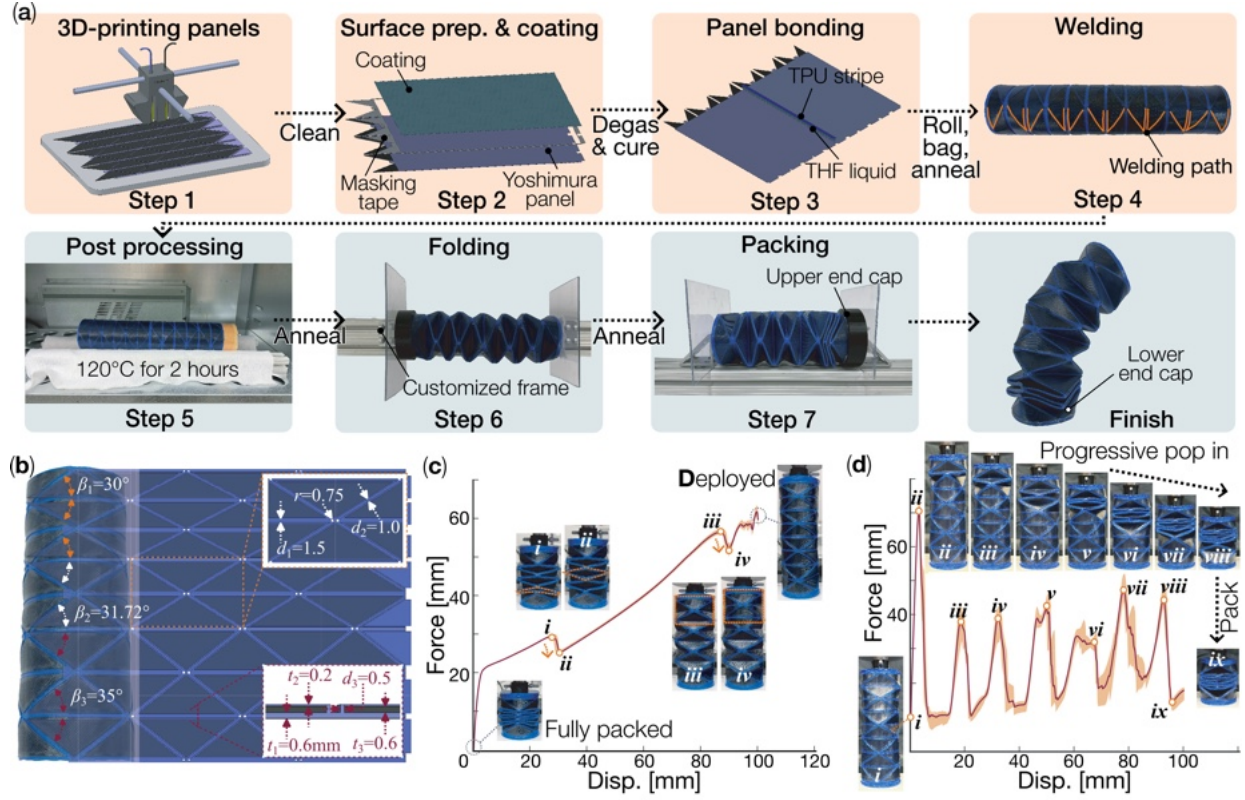


Figure 4: 3D-printed hyper-Yoshimura with a hybrid β angle design. (a) A simplified fabrication procedure of the hyper-Yoshimura specimen. Note that between steps 3 and 4, the annealing is conducted at 140°C for 5 minutes. Between steps 5, 6, and 7, the annealing is at 140°C for 2 minutes. (b) A finished prototype and its corresponding CAD model, highlight the different fabrication variables. (c, d) Mechanical extension and compression test results. The solid line is the averaged data from 7 successive loading cycles, and the shaded band is the standard deviation.

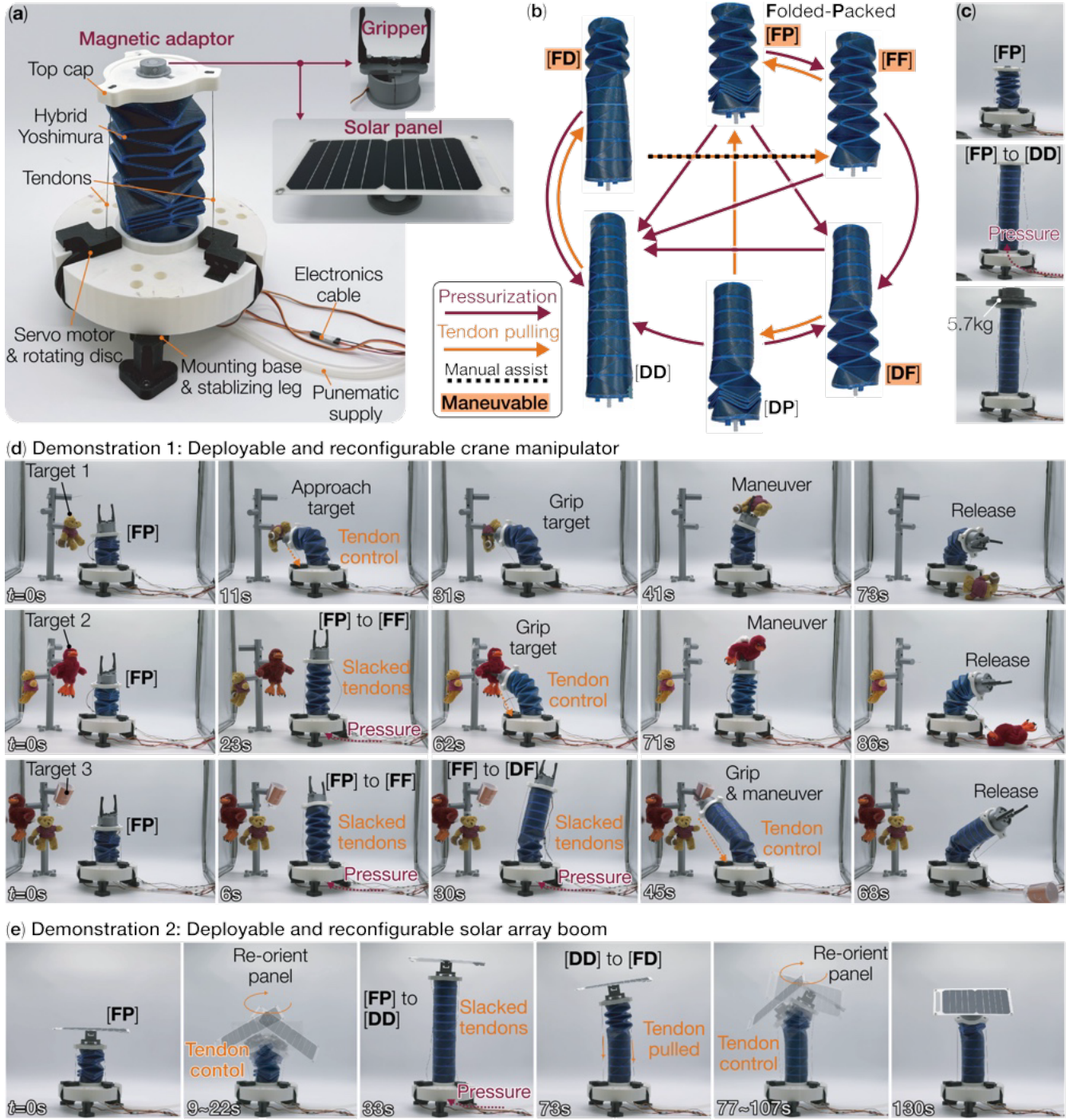


Figure 5: Robotic space crane demonstration with a hyper-Yoshimura of $\beta = 31.72^\circ, 35^\circ$, $n = 3$, and $m = 6$. (a) The complete robotic demonstration setup highlighting the pneumatic and tendon actuation and two hot-swappable end attachments: a gripper and a solar panel. (b) The switching sequence among all six possible configurations. Note that four of them are maneuverable (or bendable) by tendon control. (c) The load-bearing capacity of Deployed hyper-Yoshimura is sufficient to carry 28.5 times its structure weight. (d) Deployable manipulation demonstration with an expandable workspace. (e) Solar panel reorientation demonstration.

Mode	States	β	θ_{in}	θ_{out}	γ	d	ζ	ψ
Symmetric	Deployed	$(0^\circ, 90^\circ)$	180°	180°	0°	w	180°	0°
	Folded	$\left[\frac{90^\circ}{n}, 90^\circ\right)$	$\sin^{-1}\left(\frac{2d}{w} \tan \frac{90^\circ}{n}\right)$	$\sin^{-1}\left(\frac{2d}{w} \tan \frac{90^\circ}{n}\right)$	0°	$w \sin\left(\frac{\theta}{2}\right)$	180°	0°
	Self-Packed	$\left[\frac{90^\circ}{n}, 45^\circ\right]$	0°	0°	0°	0	$\cos^{-1}\left(\frac{2 \sin^2\left(\frac{90^\circ}{n}\right)}{\sin^2 \beta} - 1\right)$	0°
Asymmetric	Edge-wise Degeneracy	$[\beta_{in}, 45^\circ]$	$\geq 0^\circ$	$\theta_{out}(n, \beta_{in}, \theta_{in})$	$2 \sin^{-1}\left(\frac{w}{2\lambda'}\right)$	$\frac{\sin\left(\frac{\gamma}{2}\right)}{w}$	180°	$\frac{360^\circ}{n}i + \frac{180^\circ}{n}$
	Vertex-wise Degeneracy	$[\beta_{out}, 45^\circ]$	$\theta_{in}(n, \beta_{out}, \theta_{out})$	$\geq 0^\circ$	$2 \sin^{-1}\left(\frac{w}{2\lambda}\right)$	$\frac{\sin\left(\frac{\gamma}{2}\right)}{\sin\left(\frac{180^\circ}{n}\right)}$	180°	$\frac{360^\circ}{n}i$

Table 1: Summary of the geometric design parameters corresponding to the metastable states of the structure, classified into symmetric and asymmetric configurations. Each deployment mode is associated with specific values or analytical expressions for key geometric variables, including the sector angle (β), in-plane and dihedral angles ($\theta_{in}, \theta_{out}$), tilt angle (γ), slant height (d), out-of-plane hyper-fold angle (ζ), and phase angle (ψ). The functions $\theta_{in}(n, \beta, \theta_{out})$ and $\theta_{out}(n, \beta, \theta_{in})$ are evaluated using the analytical relationships derived in Section 1 of the supplementary text.

References and Notes

1. L. Puig, A. Barton, N. Rando, A review on large deployable structures for astrophysics missions. *Acta astronautica* **67** (1-2), 12–26 (2010).
2. J. Santiago-Prowald, H. Baier, Advances in deployable structures and surfaces for large apertures in space. *CEAS Space Journal* **5** (3), 89–115 (2013).
3. S. Seo, M.-W. Han, A Review on Deployable Structures in Space Industry. *International Journal of Precision Engineering and Manufacturing-Smart Technology* **3** (1), 83–96 (2025).
4. M. Schenk, A. D. Viquerat, K. A. Seffen, S. D. Guest, Review of inflatable booms for deployable space structures: packing and rigidization. *Journal of Spacecraft and Rockets* **51** (3), 762–778 (2014).
5. F. Zhang, *et al.*, Rapidly deployable and morphable 3D mesostructures with applications in multimodal biomedical devices. *Proceedings of the National Academy of Sciences* **118** (11), e2026414118 (2021).
6. F. Bobbert, S. Janbaz, A. Zadpoor, Towards deployable meta-implants. *Journal of Materials Chemistry B* **6** (21), 3449–3455 (2018).
7. J. Gafford, *et al.*, Shape deposition manufacturing of a soft, atraumatic, deployable surgical grasper. *Journal of Medical Devices* **8** (3), 030927 (2014).
8. I. Doroftei, I. A. Doroftei, Deployable structures for architectural applications-a short review. *Applied mechanics and materials* **658**, 233–240 (2014).
9. G. E. Fenci, N. G. Currie, Deployable structures classification: A review. *International journal of space structures* **32** (2), 112–130 (2017).
10. E. R. Adrover, E. Rivas-Adrover, *Deployable structures* (Laurence King Publishing) (2015).
11. S.-J. Kim, D.-Y. Lee, G.-P. Jung, K.-J. Cho, An origami-inspired, self-locking robotic arm that can be folded flat. *Science Robotics* **3** (16), eaar2915 (2018).

12. C. Kim, *et al.*, Inflatable robotics arm capable of deploying and retracting by rolling for high-packaging ratio, in *2024 IEEE 7th International Conference on Soft Robotics (RoboSoft)* (IEEE) (2024), pp. 990–996.
13. G. He, C. Sparks, N. Gravish, Grasping and rolling in-plane manipulation using deployable tape spring appendages. *Science Advances* **11** (15), eadt5905 (2025).
14. D.-Y. Lee, J.-K. Kim, C.-Y. Sohn, J.-M. Heo, K.-J. Cho, High-load capacity origami transformable wheel. *Science Robotics* **6** (53), eabe0201 (2021).
15. Z. Zhakypov, C. H. Belke, J. Paik, Tribot: A deployable, self-righting and multi-locomotive origami robot, in *2017 IEEE/RSJ International Conference on Intelligent Robots and Systems (IROS)* (IEEE) (2017), pp. 5580–5586.
16. W. Wang, N.-G. Kim, H. Rodrigue, S.-H. Ahn, Modular assembly of soft deployable structures and robots. *Materials horizons* **4** (3), 367–376 (2017).
17. Z. Zhakypov, K. Mori, K. Hosoda, J. Paik, Designing minimal and scalable insect-inspired multi-locomotion millirobots. *Nature* **571** (7765), 381–386 (2019).
18. A. Sedal, A. H. Memar, T. Liu, Y. Mengüç, N. Corson, Design of deployable soft robots through plastic deformation of kirigami structures. *IEEE Robotics and Automation Letters* **5** (2), 2272–2279 (2020).
19. F. Fuentes, L. H. Blumenschein, Deployable robotic structures via passive rigidity on a soft, growing robot, in *2023 IEEE International Conference on Soft Robotics (RoboSoft)* (IEEE) (2023), pp. 1–7.
20. P. Bosscher, R. L. Williams, M. Tummino, A concept for rapidly-deployable cable robot search and rescue systems, in *International Design Engineering Technical Conferences and Computers and Information in Engineering Conference*, vol. 47446 (2005), pp. 589–598.
21. M. Runciman, J. Avery, M. Zhao, A. Darzi, G. P. Mylonas, Deployable, variable stiffness, cable driven robot for minimally invasive surgery. *Frontiers in Robotics and AI* **6**, 141 (2020).

22. P. Palmieri, *et al.*, A deployable and inflatable robotic arm concept for aerospace applications, in *2021 IEEE 8th International Workshop on Metrology for AeroSpace (MetroAeroSpace)* (IEEE) (2021), pp. 453–458.
23. M. Park, *et al.*, Deployable soft origami modular robotic arm with variable stiffness using facet buckling. *IEEE Robotics and Automation Letters* **8** (2), 864–871 (2022).
24. L. H. Blumenschein, L. T. Gan, J. A. Fan, A. M. Okamura, E. W. Hawkes, A tip-extending soft robot enables reconfigurable and deployable antennas. *IEEE Robotics and Automation Letters* **3** (2), 949–956 (2018).
25. Y. Yoshimura, *On the mechanism of buckling of a circular cylindrical shell under axial compression*, Tech. rep. (1955).
26. Q. Zhang, H. Fang, J. Xu, Yoshimura-origami based earthworm-like robot with 3-dimensional locomotion capability. *Frontiers in Robotics and AI* **8**, 738214 (2021).
27. J. Cai, X. Deng, Y. Xu, J. Feng, Motion analysis of a foldable barrel vault based on regular and irregular Yoshimura origami. *Journal of Mechanisms and Robotics* **8** (2) (2016).
28. S. Seo, W. Park, D. Lee, J. Bae, Origami-structured actuating modules for upper limb support. *IEEE Robotics and Automation Letters* **6** (3), 5239–5246 (2021).
29. Q. Zhang, H. Fang, J. Xu, Tunable dynamics in Yoshimura origami by harnessing pneumatic pressure. *Journal of Sound and Vibration* **544**, 117407 (2023).
30. A. Micheletti, I. Giannetti, G. Mattei, A. Tiero, Kinematic and static design of rigid origami structures: Application to modular yoshimura patterns. *Journal of Architectural Engineering* **28** (2), 04022009 (2022).
31. S. Yoo, J. Kim, J. Park, Y. Cha, Design and analysis of origami-based multimodal actuator capable of linear and bending motion. *IEEE Robotics and Automation Letters* **9** (1), 151–158 (2023).
32. S. Li, H. Fang, S. Sadeghi, P. Bhovad, K.-W. Wang, Architected origami materials: how folding creates sophisticated mechanical properties. *Advanced materials* **31** (5), 1805282 (2019).

33. E. T. Filipov, T. Tachi, G. H. Paulino, Origami tubes assembled into stiff, yet reconfigurable structures and metamaterials. *Proceedings of the National Academy of Sciences* **112** (40), 12321–12326 (2015).
34. E. Filipov, K. Liu, T. Tachi, M. Schenk, G. H. Paulino, Bar and hinge models for scalable analysis of origami. *International Journal of Solids and Structures* **124**, 26–45 (2017).
35. V. Deshpande, Y. Phalak, Z. Zhou, I. Walker, S. Li, ‘Golden Ratio Yoshimura’ for meta-stable and massively reconfigurable deployment. *Philosophical Transactions A* **382** (2283), 20240009 (2024).
36. T. H. Cormen, C. E. Leiserson, R. L. Rivest, C. Stein, *Introduction to algorithms* (MIT press) (2022).
37. R. Dechter, J. Pearl, Generalized best-first search strategies and the optimality of A. *Journal of the ACM (JACM)* **32** (3), 505–536 (1985).
38. R. Bellman, Dynamic programming. *science* **153** (3731), 34–37 (1966).
39. J. Choo, *et al.*, Simulation-guided beam search for neural combinatorial optimization. *Advances in Neural Information Processing Systems* **35**, 8760–8772 (2022).
40. D. Tiffin, M. Mahlin, Tall Lunar Towers: Systems Analysis of Lunar-Surface-Assembled Power, Communication, and Navigation Infrastructure, in *ASCEND 2023*, p. 4754 (2023).
41. K. Song, M. Mikulas, M. K. Mahlin, J. T. Cassady, Sizing and design tool for tall lunar tower, in *AIAA SciTech 2023 Forum* (2023), p. 0382.
42. T. Amadeo, *et al.*, Soft robotic deployable origami actuators for neurosurgical brain retraction. *Frontiers in Robotics and AI* **8**, 731010 (2022).
43. S. Leanza, S. Wu, X. Sun, H. J. Qi, R. R. Zhao, Active materials for functional origami. *Advanced Materials* **36** (9), 2302066 (2024).
44. D. Rus, M. T. Tolley, Design, fabrication and control of origami robots. *Nature Reviews Materials* **3** (6), 101–112 (2018).

45. S. Li, D. M. Vogt, D. Rus, R. J. Wood, Fluid-driven origami-inspired artificial muscles. *Proceedings of the National academy of Sciences* **114** (50), 13132–13137 (2017).
46. S. Li, K. Wang, Fluidic origami with embedded pressure dependent multi-stability: a plant inspired innovation. *Journal of The Royal Society Interface* **12** (111), 20150639 (2015).

Acknowledgments

Funding: Z. Z., Y. P., E. B., and S. L. acknowledge the gracious support from National Science Foundation (CMMI-2240211 and 2312422). V. D acknowledges the gracious support from Virginia Tech (Hord fellowship and graduate student assistantship) I. W. acknowledges the gracious support of the National Science Foundation (CMMI-2312423 and HCC-2221126).

Author contributions: S. L. and I. W. conceived the concept the mentored the research effort. Z. Z. fabricated and tested the hyper-Yoshimura space crane concept. Y. P. and V. D. formulated the geometry and kinematics models of hyper-Yoshimura. Z. Z., E. B., and Y. P. fabricated and tested the cellphone charging station concept. All contributed to the writing and editing of this manuscript. Use initials to abbreviate author names.

Competing interests: There are no competing interests to declare.

Data and materials availability: All data are included in the main text and supplementary sections of this paper.

Supplementary materials

Supplementary Text

Figs. S1 to S9

Tables S1 to S2

Movie S1 to S9

References (7-46)